Millimeter-Wave Urban Celluar Channel Characterization and Recipe for High-Precision Site-Specific Channel Simulation

Hibiki Tsukada, *Member, IEEE,* Naoya Suzuki, Banibrata Bag, *Member, IEEE,* Riku Takahashi,and Minseok Kim, *Senior Member, IEEE,*

***Abstract*—To design a reliable communication system utilizing millimeter-wave (mm-wave) technology, which is gaining popularity due to its ability to deliver multi-gigabit-per-second data rate, it's essential to consider the site-specific nature of the mm-wave propagation. Conventional site-general stochastic channel models are often unsatisfactory for accurately reproducing the channel responses under specific usage scenarios or environments. For high-precision channel simulation that reflects site-specific characteristics, this paper proposes a channel model framework leveraging a widely accepted 3GPP map-based hybrid channel modeling approach, and it provides a detailed recipe to apply it to an actual scenario using some examples. First, an extensive measurement campaign was conducted in typical urban macro and micro cellular environments using an in-house dual-band (24/60 GHz) double-directional channel sounder. Subsequently, the mm-wave channel behavior was characterized, focusing on the difference between the two frequencies. Then, the site-specific large-scale and small-scale channel properties were parameterized. As an essential component for improving prediction accuracy, this paper proposes an exponential decay model for power delay characteristics of non-line-of-sight clusters, of which deterministic prediction tools significantly overestimate powers. Finally, using the in-house channel model simulator (CP-SQDSIM) developed for grid-wise channel data (PathGridData) generation, a significant improvement in prediction accuracy compared with the existing 3GPP map-based channel model was demonstrated.**

***Index Terms*—millimeter wave (mm-wave), 5G mobile communication, hybrid channel model, outdoor urban radio channels, channel model simulator, wireless emulator**

I. Introduction

With a projected 50 billion devices worldwide by 2030, communication between them is more prevalent than ever. This surge in traffic volume leads to spectral efficiency degradation and frequency spectrum congestion, and mutual interference is predicted to become even more severe. Therefore, to address these challenges and meet the ever-increasing demand for improving data rates as well as personalized experiences concerning quality-of-services (QoS), utilizing the millimeter-wave (mm-wave) band is indispensable. The new radio access technology (RAT) using mm-wave bands (24—71 GHz has been identified for IMT frequencies in WRC-19) can provide enormous bandwidth, low latency, and ultra-high data rate in the range of Gbps, which makes mm-wave technology suitable for a variety of advanced services and future applications. However, while mm-wave bands offer various advantages mentioned above, the current fifth-generation (5G) technology is still struggling to utilize them entirely due to their unique propagation characteristics, which differ significantly from those of low-frequency bands [1].

The development of accurate channel models reflecting diverse effects of specific usage scenarios or environments requires the collection of a large amount of measurement data in various scenarios and frequencies. To date, numerous research groups and organizations worldwide have undertaken campaigns to measure radio characteristics across a wide range of mm-wave bands and in different scenarios. For example, extensive propagation measurements in both outdoor and indoor urban environments at various frequencies, including 28 GHz, 38 GHz, 60 GHz, and 73 GHz, were conducted [1]–[3], and mm-wave propagation channel characteristics in urban scenarios at 28 GHz were investigated [4], [5]. Many other groups [6]–[8] are similarly involved in measurement campaigns investigating mm-wave propagation channel characteristics in various scenarios and channel parameters for new wireless communication technologies such as beamforming, massive MIMO, etc.; these efforts contribute to developing a suitable channel model for 5G or beyond wireless communication systems [9]–[13]. However, further study, such as site-specific behavior and frequency-dependent characteristics, should be explored to make full use of the mm-wave bands.

Again, the utilization of mm-wave bands can realize a significantly higher data rate owing to its abundant unexploited bandwidth. However, the coverage area of these bands is usually limited due to the extremely large propagation loss [14], [15]. Furthermore, the propagation characteristics in mm-wave bands are highly dependent on the environment, and the communication link easily gets blocked by small obstacles, such as trees, cars, signboards, etc, in the street. In addition, the mm-wave signal gets diffused through scattering by a very tiny object or rough surfaces of a large object [14]–[16]. Consequently, existing channel models designed for low-frequency bands cannot satisfactorily predict the propagation channel's behavior with high precision for the mm-wave bands. Therefore, it is crucial to develop a more suitable channel model for mm-wave new RATs [17], considering a balanced approach between the computational complexity

H. Tsukada, N. Suzuki, B. Bag, R. Takahashi and M. Kim are with the Graduate School of Science and Technology, Niigata University, Niigata 950-2181, Japan (e-mail: mskim@eng.niigata-u.ac.jp).

H. Tsukada is currently with NTT Access Network Service Systems Laboratories.

Manuscript received April 19, 2005; revised August 26, 2015.

and the prediction accuracy. Additionally, a simulation tool is necessary for system verification and evaluation.

In recent years, various organizations and research communities have developed different approaches for designing and simulating channel models for cellular networks and local area networks (LANs). Some widely accepted channel models are 3GPP [18], [19], WINNER [20], COST2100 [21], METIS [22], QuaDRiGa [23], NYUSIM [12], and MiWEBA [24], [25]. Although these channel modeling approaches have their own standards that emphasize their priorities and uniqueness, they sometimes coincide with other methods. However, the channel models can broadly be categorized into stochastic, deterministic, and hybrid channel models. The stochastic channel model approach, the so-called geometry-based stochastic channel model (GSCM), such as WINNER, 3GPP, COST2100, and so forth, has been widely accepted for conventional wireless communication systems due to its ease of implementation. However, it cannot provide high-precision reproducibility capturing the effects of specific usage scenarios or environments in mm-wave new RATs [3]. Meanwhile, the deterministic channel model approach, such as a ray tracing (RT) based modeling, utilizes a delicate or simplified 3D geometric description of the propagation environment to produce channel responses in a specific environment [26]–[29]. Although these approaches are promising for accurate site-specific predictions, they are not always convenient due to their computational complexity and limited accuracy when obtaining complex microscopic interactions for a large-scale propagation area [11], [30]–[32].

To compensate for the weaknesses of stochastic and deterministic channel models, a combination of both descriptions, so-called hybrid channel models, have also been developed to simplify the modeling of complex scattered multipaths while preserving accuracy in environment-specific paths by specular reflections. This allows for incorporating deterministic components induced by significantly large environmental objects such as ground, trees, and building walls, as well as non-deterministic components originating from random, uncommon, and small indoor or outdoor objects whose positions are difficult to predict. Some well-known hybrid channel models are QuaDRiGa [33], 3GPP map-based model [19], and Q-D channel model [34], [35]. In these models, obtaining the deterministic components using the ray tracing method is straightforward, but incorporating the attenuation caused by diffuse scattering in mm-wave propagation into the channel model is challenging. To address this issue, the ray tracing calibration method is proposed to incorporate various types of diffuse scattering models in ray tracing calculation [36]. However, this kind of approach can not be very practical due to the difficulty of the complicated setup of the model. In [36], ray tracing results are compensated with object-specific diffuse scattering models against individual rays by distinguishing surface materials of the 3D model and setting scattering parameters for each material. However, it is not practical due to the difficulty of the complicated setup in the model of a macro environment. Therefore, this paper suggests a calibration method using an exponential decay model for power delay characteristics of non-line-of-sight (NLoS) clusters, which is a novel and feasible idea to incorporate the non-negligible effects of diffuse scattering into the deterministic components to improve the accuracy.

Before implementing a new wireless communication system, it is essential to thoroughly analyze the site-specific propagation behaviors and assess its link-level and system-level performances. However, conducting large-scale system verification with advanced radio equipment and wireless technology by deploying hundreds of wireless devices in the target area can be time-consuming and expensive. Furthermore, this approach may not ensure reproducibility due to possible changes in environment and condition, rendering it impractical. Thus, it is crucial to develop a high-precision radio wave simulator/emulator that can accurately estimate and verify new radio propagation behaviors, which significantly reduces the time and costs associated with the process while allowing for variations in scenarios, network layouts, and other required specifications [37]. Therefore, this study considers a hybrid channel model with site-specific channel representation (SSCR) exploiting geometric information of specific environments, such as 2D maps and 3D CAD data for high-precision channel simulation.

A. Contributions

As described above, this paper proposes a Q-D channel model framework for high-precision channel simulation reflecting site-specific characteristics, leveraging a widely accepted 3GPP map-based hybrid channel modeling approach. Specifically, to improve prediction accuracy, a calibration method of deterministic components is proposed. It also provides a detailed recipe for applying it to an actual scenario. The paper's primary contributions are described as follows:

- An extensive double-directional (D-D) channel measurement campaign in typical urban cellular environments (urban macrocell (UMa) and microcell (UMi)) at two different carrier frequencies (24 and 60 GHz) using an in-house channel sounder was conducted. Most of the existing multi-frequency measurements were sequentially conducted at a single frequency, and dual-frequency simultaneous measurements are scarce. Joint clustering with composite datasets of 24 and 60 GHz, which can extract common clusters existing at both frequencies, enables the characterization of the cluster-level frequency-dependent behavior. From the measurement data, the site-specific channel parameters, such as large-scale parameters (LSPs) and small-scale parameters (SSPs), are extracted.
- A measurement-based exponential decay model for the power delay characteristics of non-line-of-sight (NLoS) clusters is proposed, which is essential for improving prediction accuracy. In ray tracing simulation, the powers of the NLoS clusters are significantly overestimated due to a lack of consideration of actually existing additional interaction losses caused by shadowing by small objects or diffuse scattering, which is impractical to handle deterministically. However, the proposed model can provide an efficient calibration tool for the ray-tracing

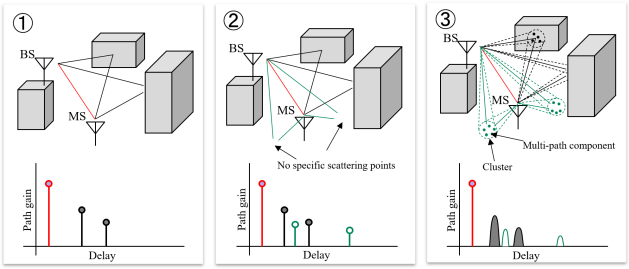

Fig. 1. Quasi-Deterministic (Q-D) channel model concept.

results, which is incorporated into the channel model to reproduce site-specific mm-wave channel characteristics more accurately.

- A high-precision site-specific channel model frameworkis developed. In this framework, deterministic paths generated by ray tracing results calibrated by using the above-mentioned proposed method and random paths generated by measured site-specific statistical parameters of LSPs and SSPs are combined to produce accurate channel responses. The spatial consistency procedure in the 3GPP model is also applied using the measured site-specific correlation distances [38]. Furthermore, an in-house channel model simulator, called CPSQDSIM, was developed for grid-wise channel data (so-called Path-GridData) generation. It can efficiently and accurately produce radio wave behaviors for any specific targeted environment.
- The proposed channel model was validated using the measured data in two different environments at carrier frequencies of 24 and 60 GHz. A comparison of the statistical characteristics of the proposed channel model with the existing 3GPP map-based channel model demonstrates a substantial improvement of the proposed model in accuracy.

B. Organisation

The subsequent parts of this paper are organized as follows: Section II provides a comprehensive description of the site-specific channel modeling concept and the methodology involved. Additionally, this section describes the channel sounder utilized during the measurement campaigns, its specifications, and the other system parameters. Section III covers the post-processing and channel characterization results. Section IV focuses on extracting channel parameters and introduces the recipe parameters to reflect site-specific characteristics, followed by Section V to describe the extension of the 3GPP map-based model. Section VI presents the channel model simulator, CPSQDSIM, and the implementation of the spatial consistency procedure. Additionally, this section presents some simulation results that intuitively demonstrate the performance of the proposed model. Finally, Section VII concludes the paper.

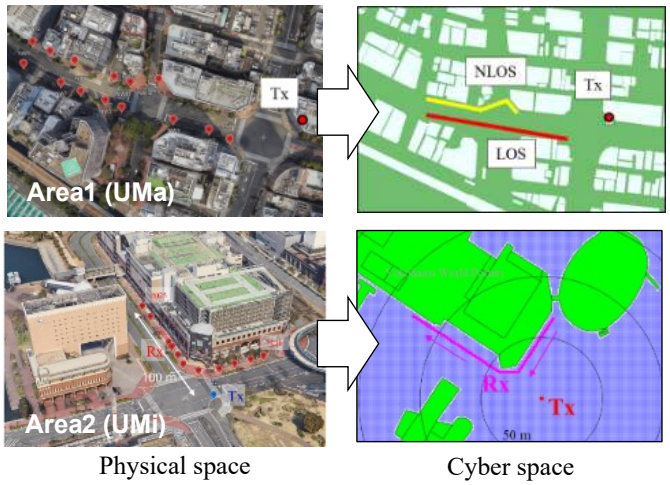

Fig. 2. Evaluation models: `Area1` (UMa) and `Area2` (UMi).

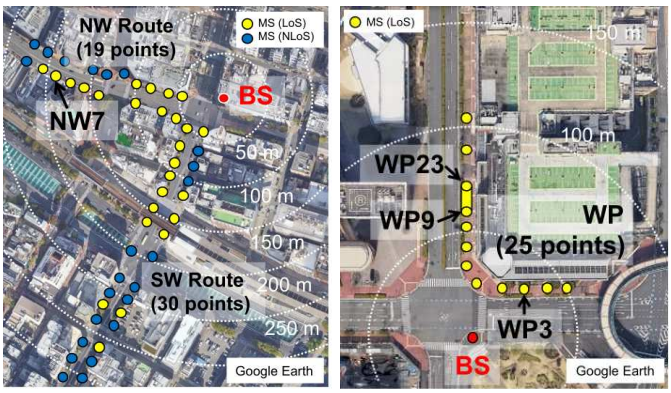

(a) `Area1` (UMa) (b) `Area2` (UMi)

Fig. 3. Measurement setup of each evaluation area.

II. Methodology

A. Site-Specific Channel Modeling Concept

This paper considers a Q-D channel model for the SSCR as illustrated in Fig. 1. Here, dominant paths are generated deterministically by simplified ray tracing in the first step. Then, the second step creates the centroids of the random clusters stochastically for the resulting channel responses to have the measured site-specific inter-cluster properties (LSPs). In the third step, the complete shape of the clusters is determined by applying the power spread stochastically, where some multipath components (MPCs) are added around each path or cluster centroid in delay and angle domains to have the measured site-specific intra-cluster properties (SSPs).

In this approach, the site-specific propagation properties in a specific environment can be well represented. Advantageously, the deterministic clusters obtained by ray tracing are inherently spatially consistent because the evolution of angles and delays are calculated based on the geometry of the environment. Further, the channel model also generates spatially consistent random clusters following the 3GPP spatial consistency procedure with measured site-specific correlation distance [38].

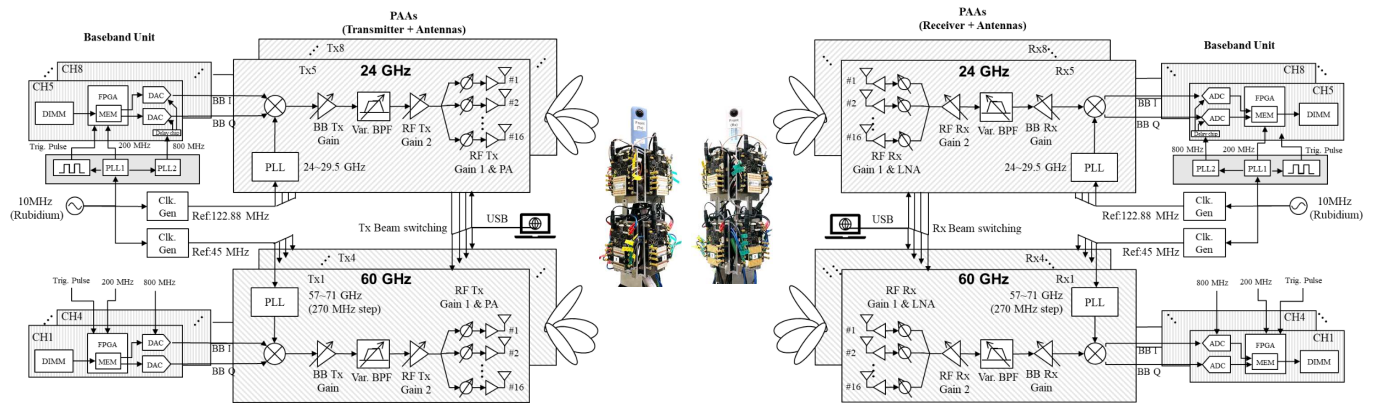

(a) Transmitter circuit (b) Receiver circuit

Fig. 4. Mm-wave dual-band (24/60 GHz) double-directional channel sounder configuration.

B. Evaluation Model Environments and Measurement Campaign

We aim to develop a radio channel simulation technique for a cyber-physical system (CPS) wireless emulator that reproduces a communication environment in a virtual space and simulates the site-specific radio propagation channels with high precision, significantly reducing the need for extensive field testing of wireless devices in real physical space [37]. In this study, the channel models are developed for two evaluation model environments in typical urban areas of Yokohama, Kanagawa, Japan: a UMa scenario around a railway station, JR Kannai (`Area1`), and a UMi scenario near a shopping mall, Yokohama World Porters (`Area2`) as shown in Fig. 2. The channel measurement campaigns were conducted in the same environments. Aerial maps of these areas, indicating the measurement points, are shown in Fig. 3.

`Area1` (UMa) involved taking measurements at 49 different points on the sidewalk as marked in Fig. 3(a) [16], [39]. The transmitter (Tx) as a base station (BS) was installed on an eight-story building roof (BS antenna height: 31.0 m), and the receiver (Rx) as a mobile station (MS) was placed at each marked point (MS antenna height: 1.5 m). The distance between the BS and MS antennas varied from 40 to 350 m. In `Area2` (UMi), measurements were taken at 25 different points on the sidewalk, as shown in Fig. 3(b) [39]. The BS antenna was mounted at 3.0 meters from the ground on the sidewalk, and the MS at each marked point had an antenna height of 1.5 meters. In Fig. 3(b), the measurement points from `WP9` to `WP23` are closely located for spatial consistency measurement [38]. The distances between the BS and MS antennas ranged from 27 to 105 m. Note that the measurement data may be subject to some influence from nearby vehicles and pedestrians at the MS locations.

C. Channel Sounding

Fig. 4 shows the in-house 24/60 GHz dual-band D-D channel sounder used in this study [39], [40]. The measurement system comprises dual-band radio frequency (RF) heads and baseband (BB) processing units. Here, the dual-band RF heads include commercial off-the-shelf (COTS)-phased array antenna beamforming transceivers (EVK02001 for 24 GHz and EVK06002 for 60 GHz, SIVERS IMA [41]). An RF head consists of four phased array antennas with 90° azimuth coverage directing toward −135°, −45°, +45°, and +135° for a full azimuth angle sweep. Stacking the 24 GHz RF heads on the 60 GHz RF heads and employing a dual 4×4 MIMO time division multiplexing (TDM) scheme realizes the simultaneous measurement of 32 channels (16 for 60 GHz and 16 for 24 GHz, respectively) [39], [40].

TABLE I
SYSTEM PARAMETERS.

Parameters	24 GHz band	60 GHz band
Carrier frequency	24.15 GHz	58.32 GHz
Signal bandwidth	200 MHz	400 MHz
Sounding signal	Multitone ($N = 512$)	Multitone ($N = 1,024$)
FFT points, N_f	2,048	2,048
Sampling rates	800 Msps	800 Msps
Delay resolution	5.0 ns	2.5 ns
Delay span	2.56 μs	2.56 μs
EIRP	32 dBm	41 dBm
HPBW	Az : 15° El: 45°	Az: 6° El @ Tx: 45° El @ Rx: 18°
Polarization	Vertical	Vertical

The 60 GHz transceiver circuit consists of a 16-element uniform linear array (ULA), whereas the 24 GHz transceiver circuit consists of a 2-by-8-element uniform planar array (UPA). Both transceivers synthesize narrow beam patterns, approximately 6° and 15° in the range of ±45° in the azimuth plane. Considering the beam's half-power beamwidth (HPBW) and beam patterns, a 90° azimuth angle sweep was achieved by using five beams for each Tx and Rx array at 24 GHz, whereas 11 beams for each Tx array and 12 beams for each Rx array at 60 GHz. Using four antenna arrays can achieve a 360° full azimuth angle sweep. The Tx power is approximately 32 and 41 dBm in terms of equivalent isotropic radiated power (EIRP) for 24 and 60 GHz, respectively. The system parameters in each frequency band are presented in TABLE I. The channel-

sounding system is elaborated in the authors' previous works [39], [40].

III. MM-WAVE DUAL-BAND CHANNEL CHARACTERIZATION

This section presents the mm-wave channel characteristics at two different frequencies obtained in the measurement campaigns conducted in the evaluation model environments [16], [38], [39] described above.

A. Post-Processing

1) Multipath component (MPC) and cluster extraction: In the measurements, band-limited, D-D angle resolved channel transfer functions (DDCTF) denoted by $H_{k,n_{\mathrm{T}},n_{\mathrm{R}}}$ were obtained. The D-D angle resolved channel impulse response (DDCIR) can be obtained by applying the Inverse Fourier Transform of the DDCTF as follows:

$$h(\check{\tau},\check{\phi}_{\mathrm{T}},\check{\phi}_{\mathrm{R}}) = \mathcal{F}^{-1}\{H(\check{f},\check{\phi}_{\mathrm{T}},\check{\phi}_{\mathrm{R}})\}, \tag{1}$$

where the delay tap is represented by $\check{\tau} \in \{n\Delta_\tau | n = 0,...,N-1\}$, where $\Delta_\tau = 1/W$, with N and W being the number of frequency tones and the bandwidth of the sounding signal (multitone), respectively. The frequency bin (tone or sub-carrier) is denoted by $\check{f} \in \{k\Delta_f | k = 0,...,N-1\}$, where $\Delta_f = W/N$. The transmitting and receiving pointing angles are represented by $\check{\phi}_{\mathrm{T}} \in \{n_{\mathrm{T}}\Delta_{\phi_{\mathrm{T}}} | n_{\mathrm{T}} = 0,...,N_{\mathrm{T}}-1\}$ and $\check{\phi}_{\mathrm{R}} \in \{n_{\mathrm{R}}\Delta_{\phi_{\mathrm{R}}} | n_{\mathrm{R}} = 0,...,N_{\mathrm{R}}-1\}$, respectively. Here, $\Delta_{\phi_{\mathrm{T}}}$ and $\Delta_{\phi_{\mathrm{R}}}$ indicate the scanning intervals of the Tx and Rx beams. Then, the D-D angular delay power spectrum (DDADPS) is obtained as

$$P(\check{\tau},\check{\phi}_{\mathrm{T}},\check{\phi}_{\mathrm{R}}) = \mathbb{E}\left\{|h(\check{\tau},\check{\phi}_{\mathrm{T}},\check{\phi}_{\mathrm{R}})|^2\right\}, \tag{2}$$

where E represents the expectation operator. After noise-filtering the DDADPS, the omnidirectional power delay profile (PDP), and the angular power spectrum (APS) are synthesized to get a visual representation of the power distribution of the delay and angular domains as

$$\mathrm{PDP}(\check{\tau}) = \sum_{\check{\phi}_{\mathrm{T}},\check{\phi}_{\mathrm{R}}} P(\check{\tau},\check{\phi}_{\mathrm{T}},\check{\phi}_{\mathrm{R}}), \tag{3}$$

$$\mathrm{APS}(\check{\phi}_x) = \sum_{\check{\tau},\check{\phi}_y} P(\check{\tau},\check{\phi}_{\mathrm{T}},\check{\phi}_{\mathrm{R}}), \tag{4}$$

where $x \in \{\mathrm{T},\mathrm{R}\}$ and $y \in \{\mathrm{T},\mathrm{R}\}\backslash x$.

In addition, the MPCs were extracted using the in-house Sub-grid CLEAN algorithm [16], [40], [42], which is a successive interference cancellation (SIC) method to obtain multipath parameters by sequentially subtracting an image of an MPC from the DDADPS in the order of the power magnitude. The replica is created from the continuous function of the beam pattern and the signal autocorrelation function [43]. In this study, the angular and delay resolutions of the Sub-grid CLEAN algorithm were set by 0.1° and 0.01 ns, respectively. Then, clustering was applied to the extracted MPCs to divide them into several groups with similar angle and delay parameters. Grouping MPCs based on similar angle and delay parameters, namely clustering, helps to identify sets of scattered waves that likely originate from the same physical objects or interactions in the environment. This approach provides a more realistic and physically meaningful model of the wireless channel. The clustering was performed on the composite datasets of the MPCs obtained at each frequency shown in Fig. 5. Here, to adjust for the increased propagation loss caused by the frequency difference, the power of each 60 GHz MPC was up-scaled by $20\log_{10}(58.32/24.15) = 7.66$ [dB]. Once clustering was completed, the clustered MPCs were separated back into their respective frequency datasets, and the power of each 60 GHz MPC was down-scaled back to its original value. This approach allowed for the identification of common clusters at both frequencies as well as uncommon (unique) clusters at either frequency. Here, we utilized the K-PowerMeans algorithm for clustering, with the number of clusters, K, manually determined by visual inspection to preserve the physical meaning of the results.

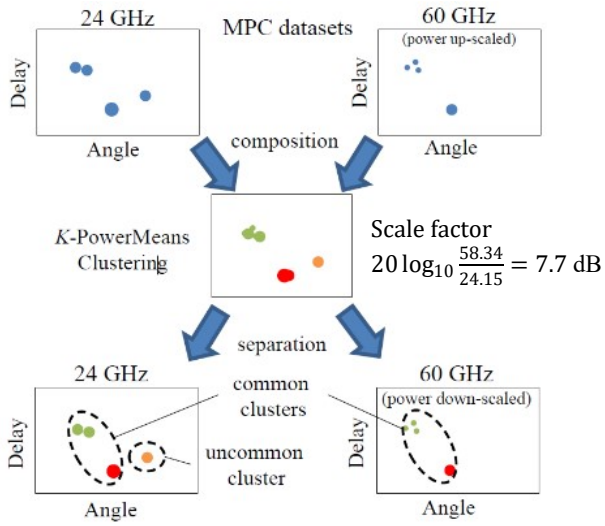

Fig. 5. Extraction of common and uncommon clusters at 24 and 60 GHz.

B. Observation of Frequency Dependence in Scattering Processes

As described above, the common clusters obtained by using two different datasets simultaneously measured at two different carrier frequencies (24 and 60 GHz) enabled some interesting observations on the cluster-level frequency-dependent behavior. Fig. 6 shows the omnidirectional PDPs obtained at `NW7` of `Area1` and `WP17` of `Area2` in as examples. Here, the cutoff level for noise-filtering for the 60 GHz band was set by the value of 7.66 dB (as much as the additional propagation loss) lower than that for the 24 GHz band to maintain the same detection range. The results of `NW7` show 13 and 5 clusters in the 24 and 60 GHz bands, respectively, with five common clusters, and those of `WP17` show 27 and 21 clusters in the 24 and 60 GHz bands, respectively, with 18 common clusters. Note that all the clusters in the 60 GHz band also exist in the 24 GHz band in `NW7`, but this is not always the case like in `WP17`. It is seen in `NW7` that several clusters with long delays exist in the 24 GHz band, whereas in the 60 GHz band, most of the clusters have short delays. That is because the clusters

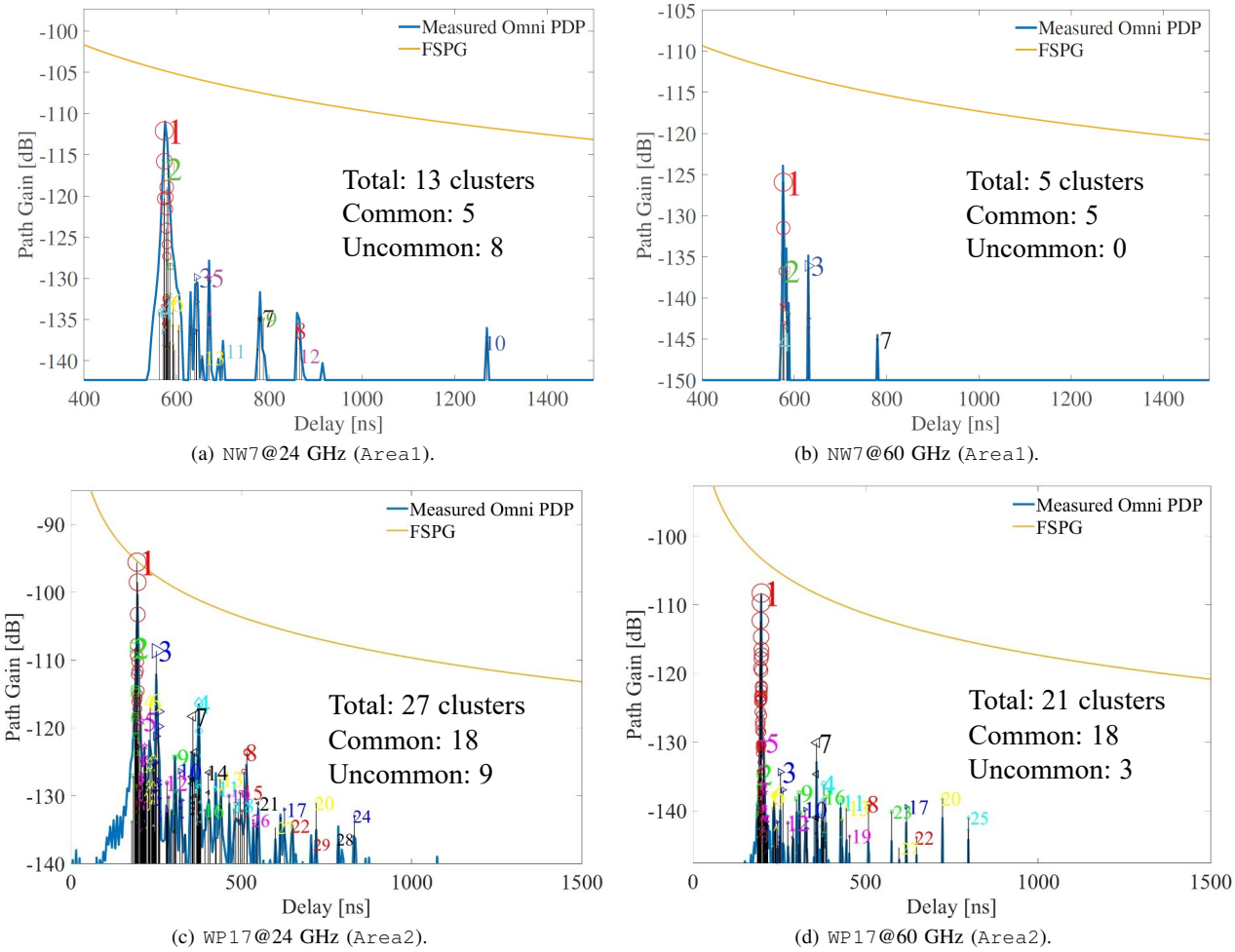

(a) NW7@24 GHz (Area1). (b) NW7@60 GHz (Area1).

(c) WP17@24 GHz (Area2). (d) WP17@60 GHz (Area2).

Fig. 6. Comparison of PDPs obtained at two different frequencies in two different environments. FSPG denotes free space path gain.

TABLE II
CHARACTERISTICS OF COMMON CLUSTERS (UNIT: DB).

	CL#	Interaction	24 GHz	60 GHz	Diff.	Excess loss
NW7	#1, #4	LoS	−108.7	−124.3	15.7	8.0
	#2	wall (SB)	−115.5	−135.9	20.4	12.7
	#3	signboard	−126.2	−134.3	8.1	0.4
	#7	walls (DB)	−131.1	−145.1	14.0	6.3
WP17	#1	LoS	−92.7	−103.0	10.3	2.6
	#3	traffic light	−107.2	−131.3	24.1	16.4
	#4	wall (SB)	−111.4	−131.5	20.1	12.4
	#6	signboard	−112.9	−132.3	19.4	11.7
	#7	wall (SB)	−112.9	−124.2	11.3	3.6

with long propagation distances are not observed in the 60 GHz band due to significant propagation loss. As can be seen from Fig. 6(b), there is only one cluster of #7 in the 60 GHz band with a longer delay than #3 due to significant attenuation, which is a significant difference from the 24 GHz band shown in Fig. 6(a). In WP17, two PDPs in Fig. 6(c) and 6(d) show similar delay distribution, but the powers of the NLoS clusters at 60 GHz significantly decreased due to additional interaction loss as in NW7.

We further investigated scattering processes from the clustering results to understand the frequency dependence of the two frequency bands. TABLE II lists some selected common clusters with the path gains, the power difference between the two frequencies, and the excess loss. The excess loss is obtained by subtracting 7.66 [dB] from the power difference. Regarding NW7, the power differences are greater than the additional propagation loss of 7.66 dB except #3. From the results, the interaction loss in the 60 GHz band is significantly greater than in the 24 GHz band. A similar trend is observed in WP17. It was also seen that the powers of NLoS clusters are significantly attenuated due to significant interaction loss by various shapes of small objects and various surface conditions of large scatterers.

C. Channel Characterization

This section provides some statistical analysis to explore more overall trends behind the measurement data.

1) Cluster Power: Fig. 7(a) depicts the cumulative distribution function (CDF) of the total cluster power, excluding the LoS power at each Rx point. Here, the values of Area1 (UMa) were adjusted by the beam pattern in the vertical plane relative to the Rx position. The average value of each frequency in the UMa scenario is −124.34 dB at 24 GHz and −115.06 dB at

60 GHz. This results in a power difference of 9.28 dB, which is 1.62 dB higher than the additional free space propagation loss (FSPL) of 7.66 dB, on average. In contrast, `Area2` (UMi) exhibits an average values of -87.18 dB and -99.27 dB at 24 and 60 GHz, respectively. This results in a power difference of 12.09 dB, which is 4.43 dB greater than the additional FSPL. This might be because of the more significant interaction loss and oxygen absorption loss in the 60 GHz band.

2) Cluster Power Difference: The CDF of the power difference between two frequencies for each common cluster across all Rx points is presented in Fig. 7(b). The results indicate that the power difference of the LoS cluster roughly equals the additional FSPL (indicated by the dashed line). However, the power of the LoS cluster is subject to fluctuations due to fading due to interference from ground reflection and possible local scattering. In `Area2` (UMi), specific points, particularly near the intersection, may partially block the first Fresnel zone by pedestrians or traffic signs and lights. The power difference distribution of the NLoS clusters is widely spread, ranging from negative to large positive values. These negative values indicate that the power is more significant in the 60 GHz band, possibly due to some interacting objects, such as curved walls and small objects around the MS. However, further investigation is needed to understand the underlying reasons. One observation for the power difference in common clusters is that it varies significantly depending on the geometry of the scatterer and the position of Tx and Rx.

3) Cluster Relative Delay: Fig. 7(c) represents the relative delay of the clusters with respect to the LoS delay. In `Area1` (UMa), the common clusters exhibit a mean relative delay of around 66 ns, implying shorter delays. The uncommon clusters at 24 GHz exhibit similar delays to those at 60 GHz in a short delay regime of about 370 ns, with the probability increasing as the delay increases. This is due to the attenuation in the 24 GHz band being less than that in the 60 GHz band, leading to having long propagation paths through multiple bounce reflections by several buildings far from the Rx. The trend in the distribution of common and uncommon clusters is also similar in `Area2` (UMi). Moreover, `Area2` had more arrival paths from scatterers far from Rx, leading to a more significant relative delay than in `Area1` (UMa), which is only surrounded by scatterers nearby Rx.

4) Cluster Number: Fig. 8 presents the number of clusters at each Rx point as a function of the Tx-Rx separation distance, along with a linear regression model obtained by the least squares method for each frequency. Both Fig. 8(a) and Fig. 8(b) indicate that the number of clusters is higher in the 24 GHz band compared to the 60 GHz band. Again, this is because the 60 GHz band experiences significantly higher interaction losses. The slope of the regression line is negative for all environments and frequencies, indicating that the number of clusters decreases as distance increases.

IV. Site-Specific Model Parameter Extraction

In this section, we describe the calculation method for extracting channel parameters and the results. In the site-specific channel model developed in this study, the channel parameters consist of LSPs and SSPs. The LSPs represent the spatiotemporal power spread of clusters, while the SSPs represent the spatiotemporal power spread of MPCs within a cluster. In the 3GPP map-based model, these parameters are defined as site-general parameters for typical categorized scenarios, such as urban and suburban areas, which are insufficient for accurately reproducing the channel responses under specific usage scenarios or environments. Therefore, this study replaces several important parameters among those defined as LSPs and SSPs in the 3GPP map-based model with the measured values, thereby deriving site-specific channel parameters. Furthermore, this section also introduces a specific set of parameters called Recipe Parameters (RPs), which are proposed to enhance the accuracy of the proposed model.

A. Large-Scale Parameters (LSPs)

According to the calculation method defined in the 3GPP model [19], the delay spread (DS) is calculated as

$$\mathrm{DS} = \sqrt{\frac{\sum_{\check{\tau}} (\check{\tau} - \mu_\tau)\mathrm{PDP}(\check{\tau})}{\sum_{\check{\tau}} \mathrm{PDP}(\check{\tau})}} \tag{5}$$

where $\mathrm{PDP}(\check{\tau})$ denotes the omnidirectional PDP obtained in (3), and the delay mean μ_τ is calculated as

$$\mu_\tau = \frac{\sum_{\check{\tau}} \check{\tau}\mathrm{PDP}(\check{\tau})}{\sum_{\check{\tau}} \mathrm{PDP}(\check{\tau})}. \tag{6}$$

Next, the azimuth spread of departure (ASD) is calculated as

$$\mathrm{ASD} = \sqrt{-2\ln\left(\left|\frac{\sum_{\check{\phi}_\mathrm{T}} \exp\left(\mathrm{j}\check{\phi}_\mathrm{T}\right)\mathrm{APS}_\mathrm{T}(\check{\phi}_\mathrm{T})}{\sum_{\check{\phi}_\mathrm{T}} \mathrm{APS}_\mathrm{T}(\check{\phi}_\mathrm{T})}\right|\right)} \tag{7}$$

where APS_T denotes the azimuth power spectrum (APS) at Tx, and is obtained in (4). The azimuth spread of arrival (ASA) can be calculated in the same way. The K-factor (K) is derived from the power ratio between the LoS path and the NLoS clusters. It is calculated as

$$K\ [\mathrm{dB}] = P^\mathrm{LoS} - 10\log_{10}\left(\sum_{j=1}^{N^\mathrm{NLoS}} 10^{\left(P_j^\mathrm{NLoS}/10\right)}\right) \tag{8}$$

where P^LoS and P_j^NLoS denote the path gains of the LoS path and NLoS clusters in dB. Additionally, j is the index of scattering clusters, taking values from 1 to N^NLoS. The delay scaling factor, r_τ, is a parameter that characterizes the power decay amount with respect to cluster delay employed in the 3GPP model. It is defined as the ratio of the average delay of NLoS clusters to DS as

$$r_\tau = \frac{\overline{\tau}}{\mathrm{DS}} \tag{9}$$

where $\overline{\tau}$ is the relative delay mean of NLoS clusters obtained as

$$\overline{\tau} = \frac{1}{N^\mathrm{NLoS}} \sum_{j=1}^{N^\mathrm{NLoS}} \left(\tau_j - \min\left(\tau_j\right)\right), \tag{10}$$

and τ_j denotes the absolute delay of the jth NLoS cluster.

Fig. 9 shows the CDFs of the LSPs obtained from the measured data in `Area1` (UMa) and `Area2` (UMi) scenarios,

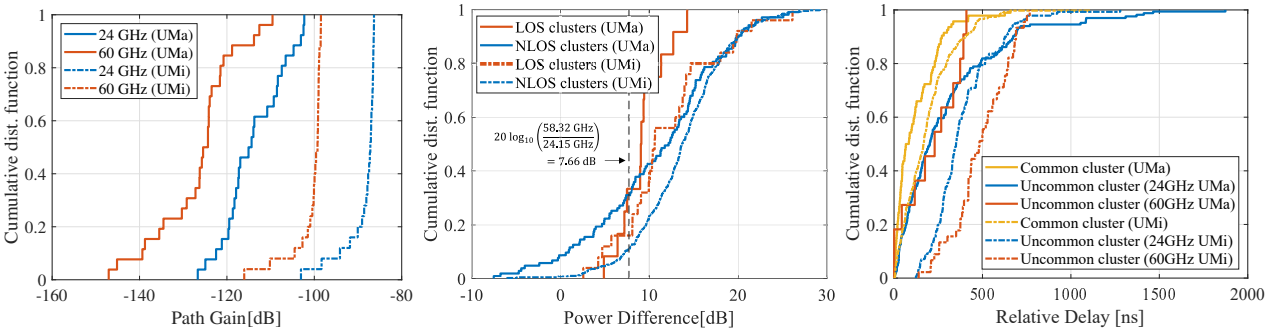

(a) Total cluster power (LoS power excluded). (b) Cluster Power difference. (c) Cluster delay.

Fig. 7. Statistical properties of clusters.

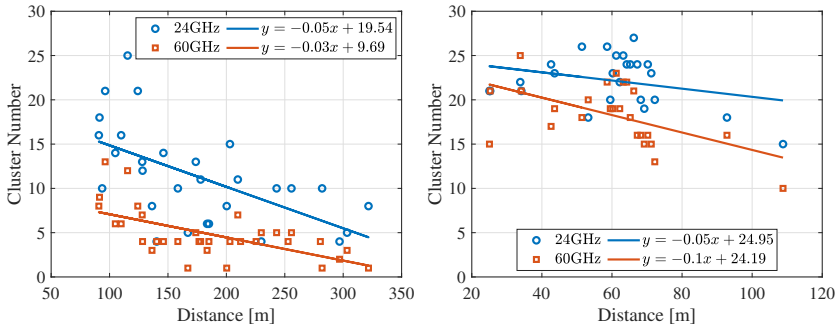

(a) `Area1` (UMa) (b) `Area2` (UMi)

Fig. 8. Cluster numbers vs. distance.

where Figs. 9(a)–9(c) are the CDFs for the 24 GHz band, and Figs. 9(d)–9(f) are those for the 60 GHz band. Each figure in Fig. 9 also included those of the 3GPP model for UMa and UMi scenarios as references. The distributions for DS in UMi and ASD in UMa, as shown in Fig. 9(d) and Fig. 9(e), respectively, are close to the reference distribution, while other parameters are significantly different from each other. This discrepancy is due to the significant impact of the surrounding environment on the propagation characteristics. From the above, it's essential to use site-specific parameters to make the channel model more adaptable to the specific environment.

Table III presents the extracted LSPs. As per the table, it is evident that although the 3GPP model suggests identical mean values of the Rician K factor for all scenarios and frequencies, the measured Rician K factor values may vary significantly for different scenarios and frequencies. Notably, the mean values of the Rician K factor at 60 GHz are higher in both environments, indicating more significant attenuation of the NLoS clusters.

B. Small-Scale Parameters (SSPs)

The intra-cluster DS (c_{DS}) and intra-cluster ASD/ASA ($c_{\mathrm{ASD/ASA}}$) are calculated as small-scale parameters, which were derived from the individual MPCs within each cluster as

$$c_{\mathrm{DS}} = \sqrt{\frac{\sum_{m=1}^{M_n}(\tau_m - \mu_\tau)^2 P_m}{\sum_{m=1}^{M_n} P_m}}, \tag{11}$$

$$c_{\mathrm{ASD/ASA}} = \sqrt{-2\ln\left(\frac{\sum_{m=1}^{M_n}\exp\left(\mathrm{j}\phi_m\right)P_m}{\sum_{m=1}^{M_n} P_m}\right)}, \tag{12}$$

where τ_m, ϕ_m, and P_m represent the delay time, departure/arrival angle (AoD or AoA), and path gain of the mth MPC, respectively, while M_n indicates the total number of MPCs belonging to the nth cluster.

The calculated SSPs are also presented in Table III. It is noteworthy that the 60 GHz band yields smaller SSP values compared to the 24 GHz band due to increased attenuation and decreased power dispersion at higher frequencies. Additionally, the measured data for c_{ASD} and c_{ASA} in both scenarios and frequencies exhibit larger values than those proposed in the 3GPP model, implying that some environmental factors may have contributed to the increased variation.

C. Recipe Parameters

In the 3GPP map-based model, deterministic clusters are generated by ray tracing. For simulation in urban environments that extend from hundreds of meters to several kilometers, a 3D model—predominantly consisting of homogeneous materials such as concrete and glass, with a simplified structure—is used. Section IV-A highlighted a significant point, namely, that the surrounding environment heavily influences the characteristics of NLoS clusters observed in the mm-wave bands. The deterministic clusters in the channel model, which are calculated on the simplified 3D model, often lead to significant differences from the measured channel responses. For a more realistic and accurate representation of

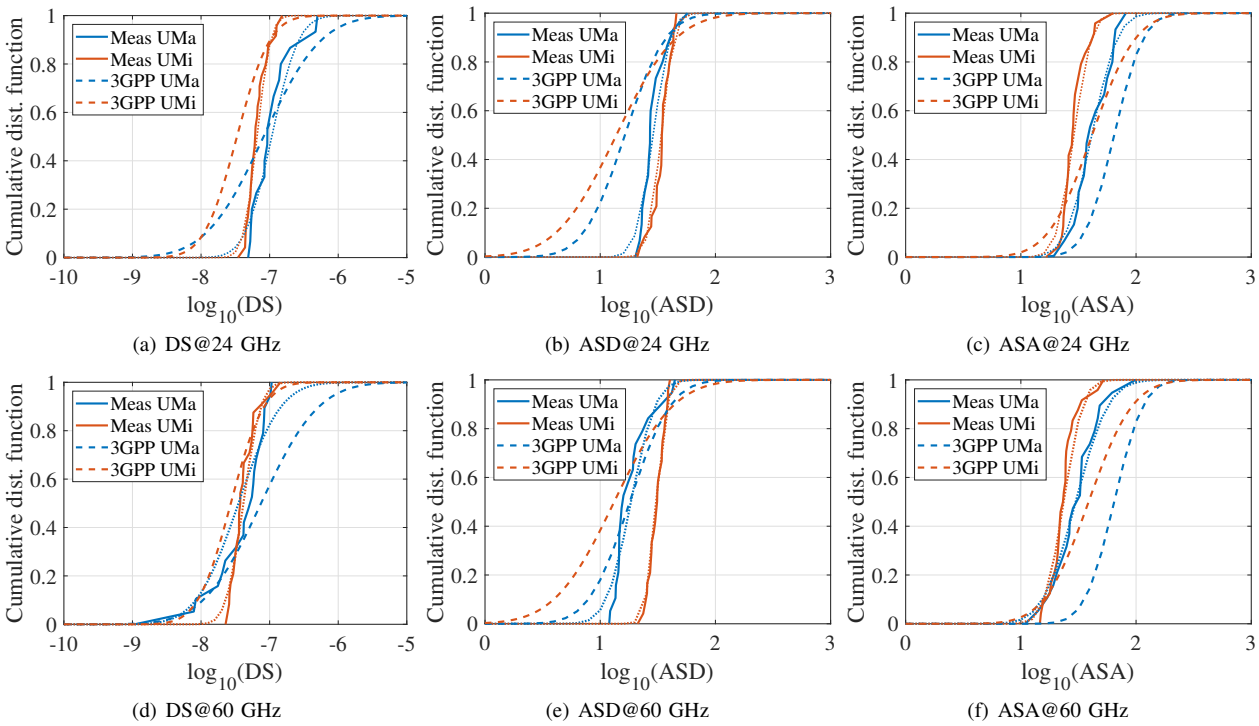

(a) DS@24 GHz (b) ASD@24 GHz (c) ASA@24 GHz

(d) DS@60 GHz (e) ASD@60 GHz (f) ASA@60 GHz

Fig. 9. Comparison between the CDFs of the LSPs obtained from the 3GPP model and the actual measured data, where 'Meas UMa' and 'Meas UMi' in the legend denote the results obtained in `Area1` and `Area2`, respectively, and the models obtained by the measurement data are also plotted in the dotted lines.

deterministic clusters, detailed information on the orientation, dimension, and dielectric properties of every building object within the evaluation area is essential. Yet, this is usually unrealistic in complex urban cellular environments with a significant separation distance between Tx and Rx. To address the mentioned challenges, this study proposes an exponential decay model for cluster power delay characteristics for the calibration of deterministic clusters as a recipe to refine the 3GPP map-based model. This model approximates the power attenuation with respect to the cluster arrival as in [44].

The exponential decay model for the power delay characteristics of NLoS clusters is expressed as

$$P(\tau)\ [\mathrm{dB}] = P_{\mathrm{m}}(\tau) + \zeta \tag{13}$$

for $0 < \tau < \tau_c$, where

$$P_{\mathrm{m}}(\tau) = P_0 + 10\log_{10}\left[\exp\left(-\frac{\tau}{\beta_0}\right)\right] \tag{14}$$

where P_0 and β_0 denote the initial path gain in dB and power decay coefficient, respectively. $\zeta \sim \mathcal{N}(0, \sigma_{\mathrm{SF}}^2)$ is a log-normal random variable where σ_{SF} denotes a standard deviation of cluster shadow fading. The following procedure calculates the model parameters. First, for each scenario and frequency, all datasets of NLoS clusters observed at every measurement point are merged. In practice, the system's noise floor usually limits the measurement's dynamic range, significantly truncating some clusters. This leads to a biased estimation of the decay model parameters. The model used only the clusters in which the delay is less than the delay threshold $\tau_c = 1.5$ μs for both frequencies. Here, the threshold indicates the value from which the probability that the cluster power becomes equal to or less than the noise level increases.

In the model parameter estimation procedure, the likelihood function is used to obtain the probability of the lth cluster being above the noise level, denoted by p_l, which is crucial because only a subset of clusters are observable in measurements. The likelihood function is formulated as follows:

$$LF = \prod_{l=1}^{L} \frac{1}{p_l \sigma_{\mathrm{SF}}\sqrt{2\pi}} \exp\left(-\frac{(P_l - P_{\mathrm{m}}(\tau_l))^2}{2\sigma_{\mathrm{SF}}^2}\right) \tag{15}$$

where τ_l and P_l denote the lth cluster's delay and power, respectively. Here, the noise path gains, P_{n}, are set by -140 dB at 24 GHz and -147.66 dB at 60 GHz. To determine the probability p_l of the lth cluster being above the noise level, the complementary error function $\mathrm{erfc}(\cdot)$ is utilized as

$$p_l = \frac{1}{2}\mathrm{erfc}\left(\frac{P_{\mathrm{n}} - P_l}{\sqrt{2}\sigma_{\mathrm{SF}}}\right). \tag{16}$$

Using (15), the corresponding log-likelihood function

$$LLF = \sum_{l=1}^{L}\left(\ln\left(p_l\sigma_{\mathrm{SF}}\right) + \frac{(P_l - P_{\mathrm{m}}(\tau_l))^2}{2\sigma_{\mathrm{SF}}^2}\right), \tag{17}$$

and the parameters are determined by minimizing LLF using the maximum likelihood estimation method as

$$(P_0^*, \beta_0^*, \sigma_{\mathrm{SF}}^*) = \arg\min_{P_0,\beta_0,\sigma_{\mathrm{SF}}} LLF \tag{18}$$

Fig. 10 presents the parameter estimation results for each scenario and frequency. The grey markers indicate the path gains of the NLoS clusters, while the red line shows the power decay line drawn by using the estimated parameters.

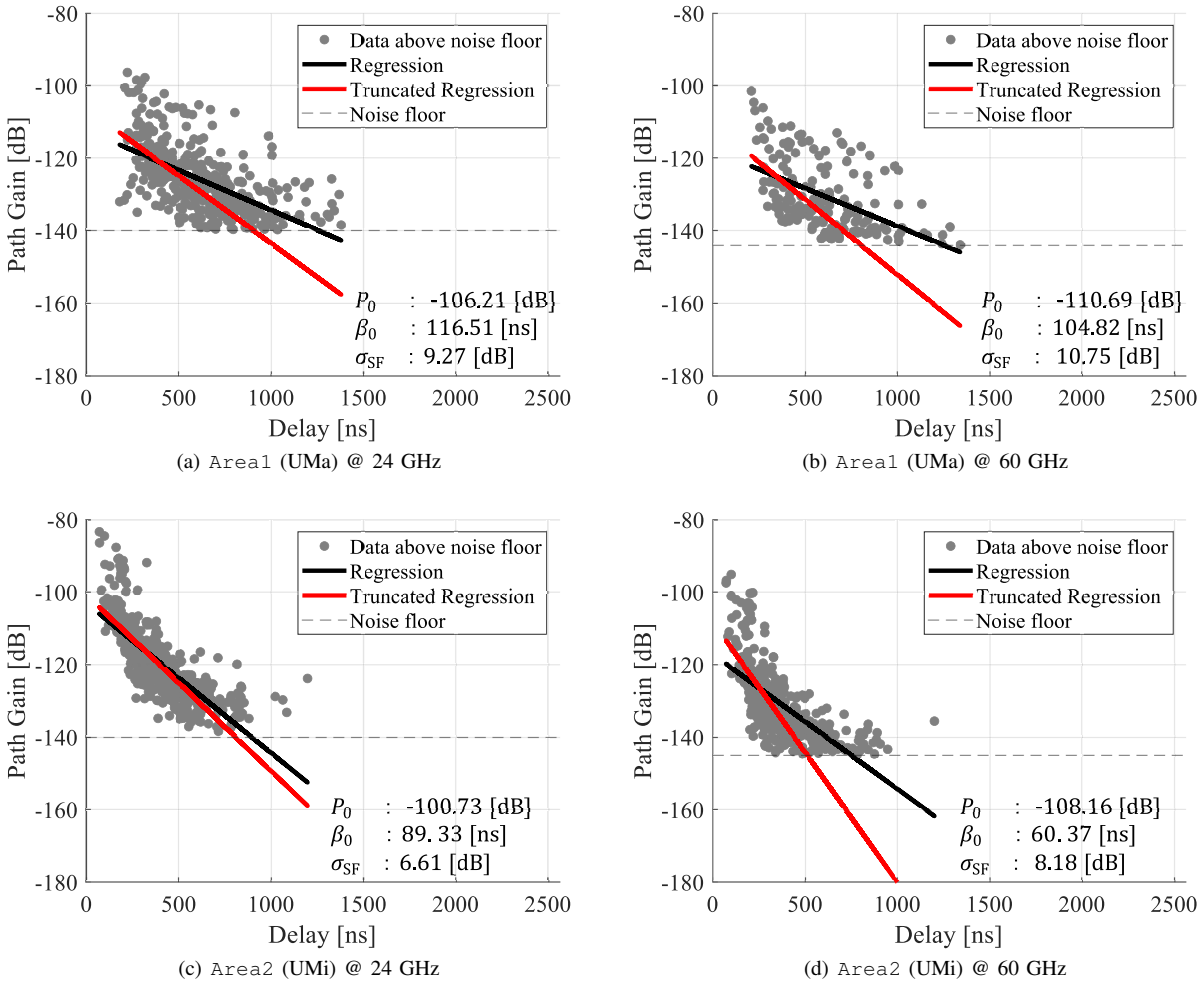

(a) `Area1` (UMa) @ 24 GHz (b) `Area1` (UMa) @ 60 GHz

(c) `Area2` (UMi) @ 24 GHz (d) `Area2` (UMi) @ 60 GHz

Fig. 10. Power delay characteristics of clusters and the exponential decay models.

The fitting results obtained without using a truncated normal distribution are also displayed in the black line for comparison. Upon comparing the results across frequencies, it is observed that β_0 at 60 GHz is smaller by 12 ns and 29 ns for UMa and UMi, respectively, compared to that at 24 GHz, indicating more significant attenuation. Furthermore, σ_{SF} is about 1.5 dB larger in both scenarios, suggesting that the propagation at the 60 GHz band is more influenced by diffused scattering by walls or small objects, and oxygen absorption than in the 24 GHz band. The dissimilarity in β_0 between scenarios also suggests that this parameter reflects specific environmental characteristics in modeling, such as the building density causing propagation interactions and variations in wall materials. Therefore, applying the exponential decay model to the calibration of the deterministic components obtained by ray tracing can efficiently represent the effects of diffuse scattering and cluster fading in the deterministic components.

V. Extension of 3GPP Map-Based Model

As described above, stochastic site-general channel models based on extensive field measurement results are usually used for medium to long-range radio propagation. However, using the site-general stochastic models limits the prediction accuracy because the channel characteristics are strongly affected by the features of the individual environment, as shown in Section IV and that has also been discussed in [43]. Therefore, a hybrid channel model that combines deterministic and stochastic descriptions, as mentioned above, emerges as an effective solution.

The 3GPP model has evolved to enable performance evaluation of new techniques through the three-dimensional (3D) extension, frequency extension above 6 GHz, and spatial consistency procedures. Further, a hybrid channel modeling framework, the 3GPP map-based model [19], is also supported. Since the 3GPP model is currently the most widely accepted standard channel model to evaluate 5G RATs, compatibility with the 3GPP in developing a channel model is important. The subsequent subsections overview the existing 3GPP map-based model and describe the proposed extension.

A. Existing framework of 3GPP Map-based model

The 3GPP map-based model is a hybrid channel model that supports frequencies from 0.5 to 100 GHz and covers eight typical scenarios, including UMi and UMa. The channel model methodology is detailed step by step in Chapter 8 of [19],

TABLE III
MODEL PARAMETERS OBTAINED FROM MEASUREMENTS (LOS)

		Area1 (UMa)		3GPP (UMa)		Area2 (UMi)		3GPP (UMi)	
		24.15 GHz	58.32 GHz	24 GHz	60 GHz	24.15 GHz	58.32 GHz	24 GHz	60 GHz
Delay spread (DS)	μ	-6.9687	-7.4543	-7.0882	-7.1250	-7.1839	-7.3825	-7.4761	-7.5656
$\log_{10}(\mathrm{DS}/1\mathrm{s})$	σ	0.31	0.49	0.66		0.16	0.20	0.38	
AOD spread (ASD)	μ	1.4597	1.2670	1.2141	1.2567	1.5286	1.4875	1.14	1.1213
$\log_{10}(\mathrm{ASD}/1^\circ)$	σ	0.12	0.17	0.28		0.09	0.07	0.41	
AOA spread (ASA)	μ	1.6154	1.4760	1.81		1.4614	1.3722	1.6180	1.588
$\log_{10}(\mathrm{ASA}/1^\circ)$	σ	0.1751	0.2230	0.20		0.1195	0.1320	0.2996	0.3048
K-factor (K) [dB]	μ	5.17	8.36	9		9.45	10.16	9	
	σ	4.63	4.60	3.5		3.38	4.37	5	
Delay scaling	μ	4.29	5.47	2.5		6.93	7.51	3	
	σ	2.23	2.81			2.72	2.77		
Cluster DS (c_{DS}) [ns]		1.87	1.03	1.85	0.54	2.57	2.26	5	
Cluster ASD (c_{ASD}) [deg.]		10.76	5.81	5		25.01	19.76	3	
Cluster ASA (c_{ASA}) [deg.]		18.26	9.13	11		26.71	22.27	17	
Initial path loss P_0 [dB]		-106.21	-110.69	–		-100.73	-108.16	–	
Power decay factor β_0 [ns]		116.51	104.82	–		89.33	60.37	–	
Cluster shadow fading σ_{SF} [dB]		9.27	10.75	–		6.61	8.18	–	

comprising 13 steps in total. *Step 1)* and *2)* discuss the setting of the environment and network layout. *Step 3)* explains the ray tracing method for generating deterministic clusters and the information required for output. *Step 4)* to *12)* describe the method for generating random clusters from channel model parameters. *Step 13)* discusses the calculation of the channel transfer function from both deterministic and random clusters. While the developed model mainly follows the aforementioned steps for compatibility, it modifies several points. The 3GPP map-based model eventually generates channel coefficients, but the developed model aims to generate a clustered MPC dataset (PathGridData) for further processing in the CPS wireless channel emulator [37].

B. Recipe for Reflecting Site-Specific Characteristics

1) Deterministic Cluster Calibration: In Section IV-C, we described the methodology for utilizing the power delay decay model of NLoS clusters as recipe parameters. This subsection elaborates on the integration of the power delay decay model into the 3GPP map-based model, which is vital to reflect the properties of the measurement environment. It discusses a method to statistically calibrate the power of deterministic clusters obtained by ray tracing on the simplified 3D model. The following step is added to *Step 3)* of the 3GPP map-based model.

Step 3+) Power compensation for NLoS deterministic clusters: The NLoS deterministic cluster power is obtained by the developed decay model as (14) for each BS-MS link. The compensation is made by using the z-score of the power deviation from the model obtained by the standardization as

$$z_{l_{\mathrm{RT}}} = \frac{\epsilon_{l_{\mathrm{RT}}} - \mu_\epsilon}{\sigma_\epsilon} \tag{19}$$

for $l_{\mathrm{RT}} = 2, \ldots, L_{\mathrm{RT}}$ (NLoS clusters). The power difference

$$\epsilon_{l_{\mathrm{RT}}} = P_{l_{\mathrm{RT}}} - P_{\mathrm{m}}(\tau_l) \tag{20}$$

where $P_{l_{\mathrm{RT}}}$ and $P_{\mathrm{m}}(\tau_l)$ denote the l_{RT}-th deterministic cluster's power and the value obtained from (14), respectively. μ_ϵ and σ_ϵ denote the mean and standard deviation of a random variable of (20), respectively. Finally, the compensated cluster's power is obtained by

$$P'_{l_{\mathrm{RT}}}\ [\mathrm{dB}] = P_0 + 10\log_{10}\left[\exp\left(-\frac{\tau_{l_{\mathrm{RT}}}}{\beta}\right)\right] + z_{l_{\mathrm{RT}}}\zeta. \tag{21}$$

2) Site-Specific Random Cluster Generation: Using site-specific LSPs and SSPs obtained by measurement, random clusters are generated following the procedures as described in [19].

VI. DEVELOPMENT AND VALIDATION OF CHANNEL MODEL GENERATOR

A. CPSQDSIM

The channel model simulator, CPSQDSIM, has been developed based on our proposed channel modeling framework, which generates a grid-wise clustered MPC dataset called PathGridData. As shown in Fig. 11, taking in deterministic cluster centroids obtained by ray tracing and site-specific statistical parameters such as LSPs and SSPs to generate random clusters, it generates the PathGridData following our proposed channel model recipe as described in Section V. The CPSQDSIM accepts any site-specific measured LSPs/SSPs dataset as user input to reproduce radio wave propagation characteristics for the targeted environment accurately.

B. Spatial Consistency

A common problem with previous drop-based stochastic channel models of microwave and mm-wave channels is that they do not allow for the temporally or spatially consistent simulation that is required in beamforming evaluation. The 3GPP model has developed a spatial consistency procedure that updates each cluster's angles and delays as the user

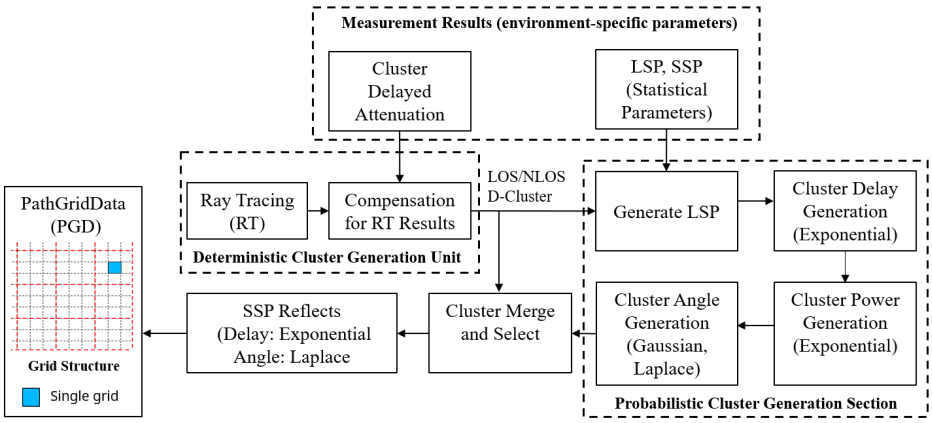

Fig. 11. Block diagram of CPSQDSIM.

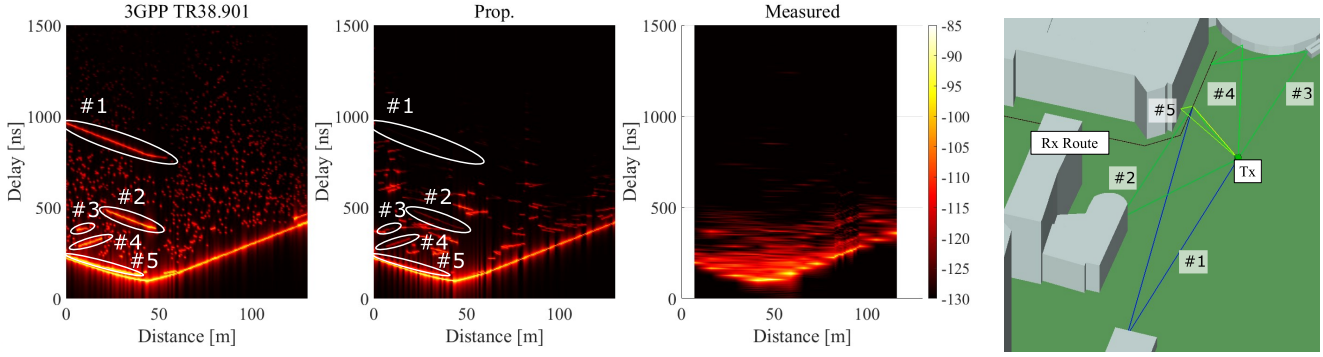

(a) PDPs

(b) Deterministic cluster generation by RT

Fig. 12. PDP characteristics with varying Rx position from WP1 to WP25, where the PDPs generated by the models were synthesized from the angle-resolved channel impulse responses reconstructed by using the measurement system's characteristics.

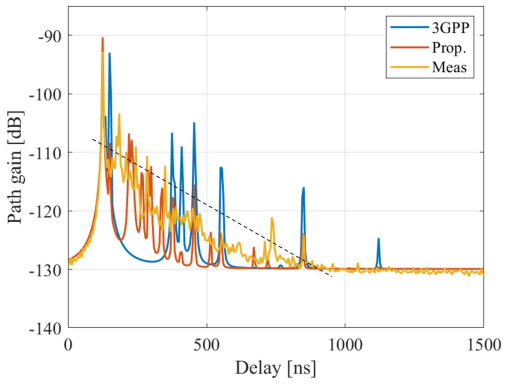

Fig. 13. PDP characteristics when Rx position is at WP3, where the PDPs generated by the models were synthesized from the angle-resolved channel impulse responses reconstructed by using the measurement system's characteristics.

moves along the path, using a linear approximation process. The spatial consistency has been implemented in CPSQDSIM using the delay and angle generation procedure described in *3GPP Spatial Consistency Procedure A*, following ***Step 5)*** and ***Step 7)***, respectively [19]. At $t_0 = 0$, when the MS/BS is initially dropped into the network, the power, delay, and angle of a spatially consistent cluster are generated. In the subsequent time step, designated as $t_k = t_{k-1} + \Delta t$, the power, delay, and angle of the clusters are recalculated, considering the MS's position in the previous time step at t_{k-1}, as well as those of the cluster at t_k, in conjunction with the MS's velocity and moving direction.

The spatial consistency procedure is applied to the random clusters by updating their delay and angle according to the direction of the Rx's movement. The birth/death for each random cluster is determined by a cluster visible region, which is generated by an exponentially distributed random variable derived from the measurements. Each cluster is updated in angle and delay domains using the *3GPP Spatial Consistency Procedure A* up to the determined cluster visible region. At the death of a random cluster, a new random cluster is generated at runtime. This procedure is repeated for all grid points traversed by the RX to generate spatially consistent channel responses. As described in Section II, the spatial consistency was measured using the setup with stationary Tx and moving Rx at approximately 1 m intervals along the direction of the arrow. Our previous investigation exhibits that for Area2, the average birth/death distance is 5.41 m and 4.16 m in the 24 and 60 GHz bands, respectively, and the analysis for Area1 can also be found in [38].

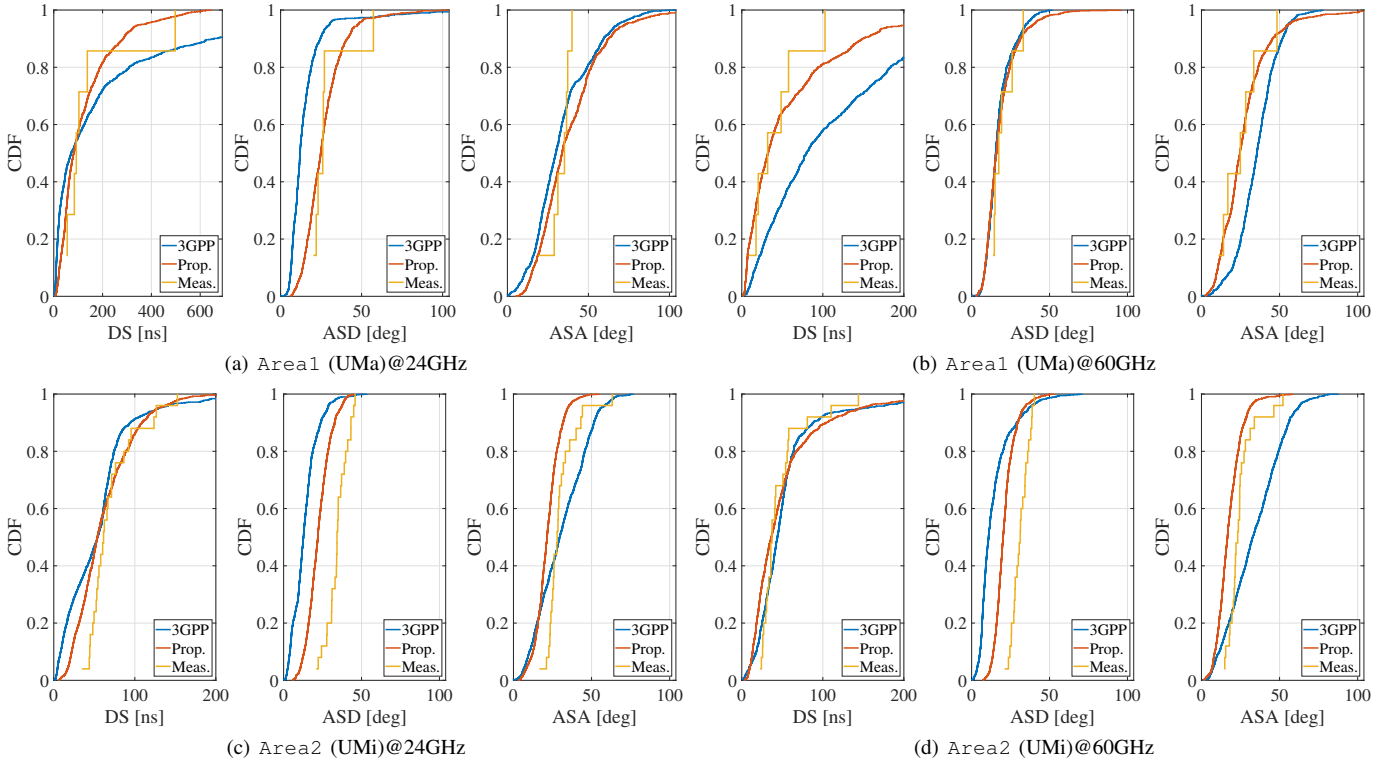

Fig. 14. Comparison of LSP (CDFs) for the 3GPP model, proposed model, and measured data at different scenarios and frequencies.

C. Validation

To verify the developed channel model, the PDP realization along the measurement route is compared. Then, the statistical properties of DS, ASD, and ASA obtained by the proposed model and the 3GPP map-based model are evaluated in terms of the measurement results. The Wireless InSite [45] was used for ray tracing calculation on the simplified 3D models of `Area1` (UMa) and `Area2` (UMi) to obtain the deterministic clusters. Here, the allowed number of reflections and diffractions was set to one. The channel parameters for random clusters are obtained from Table III. Furthermore, the RPs were applied only for the developed model.

Fig. 12 visualizes the transitions of the PDP realized along the Rx route in `Area2` obtained by the existing 3GPP map-based model (leftmost), the proposed model (center), and the measured data (rightmost), respectively, in Fig. 12(a), where a snapshot of the ray tracing simulation used for deterministic cluster generation is also provided in Fig. 12(b) for intuitive understanding of the environment. It is noted that the PDPs generated by the models were synthesized from the angle-resolved channel impulse responses reconstructed by using the measurement system's characteristics. Fig. 12(a) reveals that the existing 3GPP model exhibits extraordinarily high powers in the NLoS deterministic clusters marked in the white circles. In contrast, the proposed model describes the trend of the measurement data more closely. To be more specific, Fig. 13 displays a single PDP realized at `WP3`, of which location is indicated in Fig. 3(b). This result shows that the 3GPP map-based model significantly overestimates the NLoS cluster power, whereas the proposed model agrees well with the measurement owing to the calibration of the NLoS cluster's power. Therefore, it is seen that the proposed model ensures that the characteristics of both the deterministic cluster and random clusters agree well with the measurement.

Fig. 14 presents the CDFs of DS, ASA, and ASD obtained from `Area1` (UMa) and `Area2` (UMi) at two different frequencies of 24 and 60 GHz. Upon examining Fig. 14(a) and Fig. 14(b), it is apparent that both the DS and ASD/ASA of the proposed model at both frequencies align more closely with the measured data than the existing 3GPP model in the UMa scenario. On the other hand, regarding the UMi scenario, both the DS and ASD/ASA of the proposed model at both frequencies are closer to the measured value than the 3GPP model, as shown in Fig. 14(c) and Fig. 14(d), respectively. Since the proposed model is not a fully deterministic model but a Q-D model, it produces channel responses that are statistically similar to real-world measurements rather than exact replicas. However, even so, there is a noticeable gap between the proposed and measured distribution in the ASD of the UMi scenario at both frequencies. This is primarily attributed to the fact that the simplified 3D model could not perfectly include all dominant scattering objects that were present during the measurement. However, our future research will address this issue to improve outcomes.

VII. Conclusion

For high-precision channel simulation reflecting site-specific characteristics, this paper proposed a Q-D channel model framework. Then, a detailed recipe to apply that to two actual scenarios of `Area1` (UMa) and `Area2` (UMi) at two different mm-wave frequencies was presented. For channel modeling,

an extensive measurement campaign was conducted, and the mm-wave channel behavior was characterized, focusing on the difference between the two frequencies. The measurement results revealed that the powers of the NLoS clusters significantly decreased. This trend was more significant in the 60 GHz band than in the 24 GHz band. From the results, a measurement-based exponential decay model for power delay characteristics of NLoS clusters was proposed as an essential component for improving prediction accuracy.

In the developed channel simulation framework, deterministic paths obtained through ray tracing with calibration by the developed exponential decay model and measured site-specific statistical parameters of LSPs and SSPs are combined to generate accurate channel responses. The spatial consistency procedure in the 3GPP model was also incorporated using the measured site-specific correlation distances [38]. Furthermore, an in-house channel model simulator, CPSQDSIM, was developed for the generation of a grid-wise channel dataset, PathGridData. It can efficiently and accurately produce radio wave behaviors for any specific targeted environment.

The proposed channel model was validated using the measured data in two different environments at two different carrier frequencies of 24 and 60 GHz. The statistical validation of the proposed model compared with the existing 3GPP map-based channel model indicated a substantial improvement in accuracy.

ACKNOWLEDGEMENT

This research has been conducted under the contract "R&D for the realization of high-precision radio wave emulator in cyberspace" (JPJ000254) made with the Ministry of Internal Affairs and Communications of Japan.

REFERENCES

[1] T. S. Rappaport, S. Sun, R. Mayzus, H. Zhao, Y. Azar, K. Wang, G. N. Wong, J. K. Schulz, M. Samimi, and F. Gutierrez, "Millimeter Wave Mobile Communications for 5G Cellular: It Will Work!" *IEEE Access*, vol. 1, pp. 335–349, 2013.

[2] T. S. Rappaport, G. R. MacCartney, M. K. Samimi, and S. Sun, "Wideband Millimeter-Wave Propagation Measurements and Channel Models for Future Wireless Communication System Design," *IEEE Trans Commun*, vol. 63, no. 9, pp. 3029–3056, 2015.

[3] T. S. Rappaport, Y. Xing, G. R. MacCartney, A. F. Molisch, E. Mellios, and J. Zhang, "Overview of Millimeter Wave Communications for Fifth-Generation (5G) Wireless Networks—With a Focus on Propagation Models," *IEEE Trans. Antennas Propag.*, vol. 65, no. 12, pp. 6213–6230, 2017.

[4] J. Ko, Y. Cho, S. Hur, T. Kim, J. Park, A. F. Molisch, K. Haneda, M. Peter, D. Park, and D. Cho, "Millimeter-Wave Channel Measurements and Analysis for Statistical Spatial Channel Model in In-Building and Urban Environments at 28 GHz," *IEEE Trans. Wirel. Commun.*, vol. 16, no. 9, pp. 5853–5868, 2017.

[5] S. Hur, S. Baek, B. Kim, Y. Chang, A. F. Molisch, T. S. Rappaport, K. Haneda, and J. Park, "Proposal on Millimeter-Wave Channel Modeling for 5G Cellular System," *IEEE J Sel Top Signal Process*, vol. 10, no. 3, pp. 454–469, 2016.

[6] M. J. Kazemi, A. Abdipur and A. Mohammadi, "Indoor propagation MIMO channel modeling in 60 GHz using SBR based 3D ray tracing technique," in *2012 Proc. Second Conference on Millimeter-Wave and Terahertz Technologies (MMWaTT)*, 2012, pp. 25–28.

[7] X. Gao, O. Edfors, F. Rusek, and F. Tufvesson, "Massive MIMO Performance Evaluation Based on Measured Propagation Data," *IEEE Trans. Wirel. Commun.*, vol. 14, no. 7, pp. 3899–3911, 2015.

[8] X. Wu, C.-X. Wang, J. Sun, J. Huang, R. Feng, Y. Yang, and X. Ge, "60-GHz Millimeter-Wave Channel Measurements and Modeling for Indoor Office Environments," *IEEE Trans. Antennas Propag.*, vol. 65, no. 4, pp. 1912–1924, 2017.

[9] V. Degli-Esposti, F. Fuschini, E. M. Vitucci, M. Barbiroli, M. Zoli, L. Tian, X. Yin, D. A. Dupleich, R. Müller, C. Schneider, and R. S. Thomä, "Ray-Tracing-Based mm-Wave Beamforming Assessment," *IEEE Access*, vol. 2, pp. 1314–1325, 2014.

[10] P. Ferrand, M. Amara, S. Valentin, and M. Guillaud, "Trends and challenges in wireless channel modeling for evolving radio access," *IEEE Commun. Mag.*, vol. 54, no. 7, pp. 93–99, 2016.

[11] K. Haneda *et al.*, "5G 3GPP-Like Channel Models for Outdoor Urban Microcellular and Macrocellular Environments," in *2016 Proc. IEEE 83rd Vehicular Technology Conference (VTC Spring)*, 2016, pp. 1–7.

[12] S. Ju and T. S. Rappaport, "Millimeter-Wave Extended NYUSIM Channel Model for Spatial Consistency," in *2018 Proc. IEEE Global Communications Conference (GLOBECOM)*, 2018, pp. 1–6.

[13] S. Sun, T. S. Rappaport, M. Shafi, P. Tang, J. Zhang, and P. J. Smith, "Propagation Models and Performance Evaluation for 5G Millimeter-Wave Bands," *IEEE Trans. Veh. Technol.*, vol. 67, no. 9, pp. 8422–8439, 2018.

[14] S. Deng, G. Maccartney, and T. Rappaport, "Indoor and Outdoor 5G Diffraction Measurements and Models at 10, 20, and 26 GHz," in *Proc. IEEE Global Communications Conference (GLOBECOM)*, Dec. 2016, pp. 1–7.

[15] A. Maltsev, R. Maslennikov, A. Sevastyanov, A. Lomayev, A. Khoryaev, A. Davydov, and V. Ssorin, "Characteristics of indoor millimeter-wave channel at 60 GHz in application to perspective WLAN system," in *2010 Proc. of the Fourth European Conference on Antennas and Propagation*, 2010, pp. 1–5.

[16] M. Kim, N. Suzuki, H. Tsukada, and R. Takahashi, "Frequency Dependence of Millimeter-Wave Urban Macrocell Multipath Cluster Channels," in *2023 Proc. European Conference on Antennas and Propagation (EuCAP)*, Florence, Italy, Mar. 2023.

[17] O. O. Erunkulu, A. M. Zungeru, C. K. Lebekwe, M. Mosalaosi, and J. M. Chuma, "5G Mobile Communication Applications: A Survey and Comparison of Use Cases," *IEEE Access*, vol. 9, pp. 97 251–97 295, 2021.

[18] 3GPP, "Spatial channel model for Multiple Input Multiple Output (MIMO) simulations, Release 11," *3rd Generation Partnership Project, Tech. Rep.*, vol. 25996, Sep. 2012.

[19] "Study on channel model for frequencies from 0.5 to 100 GHz. (3GPP TR 38.901 version 16.1.0 Release 16)," (Released: Nov. 2020). [Online]. Available: https://www.etsi.org/deliver/etsi_tr/138900_138999/138901/16.01.00_60

[20] P. Kyösti, J. Meinilä, L. Hentilä, X. Zhao, T. Jämsä, C. Schneider, M. Narandzić, M. Milojević, A. Hong, J. Ylitalo, V.-M. Holappa, M. Alatossava, R. Bultitude, Y. de Jong and T. Rautiainen, "WINNER II channel models," D1.1.2 V1.2, IST-4-027756 WINNER II, Tech. Rep., 2007.

[21] L. Liu, C. Oestges, J. Poutanen, K. Haneda, P. Vainikainen, F. Quitin, F. Tufvesson, and P. Doncker, "The COST 2100 MIMO channel model," *IEEE Wirel. Commun.*, vol. 19, no. 6, pp. 92–99, Dec. 2012.

[22] L. Raschkowski, P. Kyösti, K. Kusume, T. Jämsä, V. Nurmela, A. Karttunen, A. Roivainen, T. Imai, J. Järveläinen, J. Medbo, J. Vihriälä, J. Meinilä, K. Haneda, V. Hovinen, J. Ylitalo, N. Omaki, A. Hekkala, R. Weiler, and M. Peter, *METIS Channel Models (D1.4)*, 07 2015.

[23] S. Jaeckel, L. Raschkowski, K. Börner, and L. Thiele, "QuaDRiGa: A 3-D Multi-Cell Channel Model With Time Evolution for Enabling Virtual Field Trials," *IEEE Trans. Antennas Propag.*, vol. 62, no. 6, pp. 3242–3256, 2014.

[24] R. J. Weiler, M. Peter, W. Keusgen, A. Maltsev, I. Karls, A. Pudeyev, I. Bolotin, I. Siaud and A. Ulmer-Moll , "Quasi-deterministic millimeter-wave channel models in MiWEBA," *EURASIP J. Wirel. Commun. Netw.*, vol. 84, Mar 2016. [Online]. Available: https://doi.org/10.1186/s13638-016-0568-6

[25] A. Maltsev, R. Maslennikov, A. Sevastyanov, A. Lomayev, and A. Khoryaev, "Statistical channel model for 60 GHz WLAN systems in conference room environment," in *Proc. of the Fourth European Conference on Antennas and Propagation*, 2010, pp. 1–5.

[26] H. C. Nguyen, G. R. MacCartney, T. Thomas, T. S. Rappaport, B. Vejlgaard, and P. Mogensen, "Evaluation of Empirical Ray-Tracing Model for an Urban Outdoor Scenario at 73 GHz E-Band," in *2014 Proc. IEEE 80th Vehicular Technology Conference (VTC2014-Fall)*, 2014, pp. 1–6.

[27] S. Hur, S. Baek, B. Kim, J. Park, A. F. Molisch, K. Haneda, and M. Peter, "28 GHz channel modeling using 3D ray-tracing in urban environments,"

in *2015 Proc. 9th European Conference on Antennas and Propagation (EuCAP)*, 2015, pp. 1–5.

[28] A. Schiavoni, A. Leoni, D. Arena, and R. Lanzo, "Ray tracing simulations at millimeter waves in different indoor and outdoor scenarios," in *2016 Proc. 10th European Conference on Antennas and Propagation (EuCAP)*, 2016, pp. 1–5.

[29] F. Fuschini, E. M. Vitucci, M. Barbiroli, G. Falciasecca, and V. Degli-Esposti, "Ray tracing propagation modeling for future small-cell and indoor applications: A review of current techniques," *Radio Science*, vol. 50, no. 6, pp. 469–485, 2015.

[30] Y.-G. Lim, Y. J. Cho, M. S. Sim, Y. Kim, C.-B. Chae, and R. A. Valenzuela, "Map-Based Millimeter-Wave Channel Models: An Overview, Data for B5G Evaluation and Machine Learning," *IEEE Wirel. Commun.*, vol. 27, no. 4, pp. 54–62, 2020.

[31] M. Lecci, P. Testolina, M. Polese, M. Giordani, and M. Zorzi, "Accuracy Versus Complexity for mmWave Ray-Tracing: A Full Stack Perspective," *IEEE Trans. Wirel. Commun.*, vol. 20, no. 12, pp. 7826–7841, 2021.

[32] C.-X. Wang, J. Bian, J. Sun, W. Zhang, and M. Zhang, "A Survey of 5G Channel Measurements and Models," *IEEE Commun. Surv. Tutor.*, vol. 20, no. 4, pp. 3142–3168, 2018.

[33] S. Jaeckel, L. Raschkowski, K. Börner, and L. Thiele, "QuaDRiGa: A 3-D multi-cell channel model with time evolution for enabling virtual field trials," *IEEE Trans. Antennas Propag.*, vol. 62, no. 6, p. 808–812, Jun. 2014.

[34] A. Bodi, S. Blandino, N. Varshney, J. Zhang, T. Ropitault, M. Lecci, P. Testolina, J. Wang, C. Lai, and C. Gentile, "NIST quasi-deterministic (Q-D) channel realization software documentation," Nat. Inst. Standards Technol. (NIST), Gaithersburg, MD, USA, Tech. Rep., Jan. 2021.

[35] A. Maltsev, A. Pudeyev, I. Karls, I. Bolotin, G. Morozov, R. J. Weiler, M. Peter, W. Keusgen, M. Danchenko, and A. Kuznetsov, "Quasi-deterministic approach to mmWave channel modeling in the FP7 MiWEBA project," *WWRF'33*, pp. 1–6, 2014.

[36] R. Charbonnier, C. Lai, T. Tenoux, D. Caudill, G. Gougeon, J. Senic, C. Gentile, Y. Corre, J. Chuang, and N. Golmie, "Calibration of Ray-Tracing With Diffuse Scattering Against 28-GHz Directional Urban Channel Measurements," *IEEE Trans. Veh. Technol.*, vol. 69, no. 12, pp. 14 264–14 276, 2020.

[37] "Advancement of radio wave simulation system technology in virtual space, Ministry of Internal Affairs and Communications, Japan," (Date last accessed 12-Aug-2023). [Online]. Available: https://www.tele.soumu.go.jp/j/sys/fees/purpose/emulator/index.htm

[38] N. Suzuki, H. Tsukada, R. Takahashi, B. Bag, and M. Kim, "Characterization of Spatial Consistency of Cluster Channels in Urban Environments at 24 and 60 GHz," *IEEE Antennas Wirel. Propag. Lett.*, vol. , (Accepted).

[39] M. Kim, H. Tsukada, K. Kumakura, R. Takahashi, N. Suzuki, H. Sawada and T. Matsumura, "A 24/60-GHz Dual-Band Double-Directional Channel Sounder Using COTS Phased Arrays," in *2022 Proc. IEEE International Conference on Communications (ICC)*, Seoul, Korea, May 2022.

[40] M. Kim, S. Tang, and K. Kumakura, "Fast Double-Directional Full Azimuth Sweep Channel Sounder Using Low-Cost COTS Beamforming RF Transceivers," *IEEE Access*, vol. 9, pp. 80 288–80 299, June 2021.

[41] "EVK06002/00, SIVERS IMA," (Date last accessed 12-Aug-2023). [Online]. Available: https://www.siversima.com/product/evk-06002-00/

[42] M. Kim, T. Iwata, S. Sasaki, and J. Takada, "Millimeter-Wave Radio Channel Characterization using Multi-Dimensional Sub-Grid CLEAN Algorithm," *IEICE Trans. Commun.*, vol. E103-B, no. 7, pp. 767–779, Feb 2020.

[43] H. Tsukada, K. Kumakura, S. Tang, and M. Kim, "Millimeter-Wave Channel Model Parameters for Various Office Environments," *IEEE Access*, vol. 10, pp. 60 387–60 396, June 2022.

[44] K. Haneda, J. Järveläinen, A. Karttunen, M. Kyrö, and J. Putkonen, "A Statistical Spatio-Temporal Radio Channel Model for Large Indoor Environments at 60 and 70 GHz," *IEEE Trans. on Antennas and Propag.*, vol. 63, no. 6, pp. 2694–2704, 2015.

[45] "Wireless EM Propagation Software: Wireless InSite® Remcom," (Date last accessed 4-Feb-2024). [Online]. Available: https://www.remcom.com/wireless-insite-em-propagation-software

Hibiki Tsukada received the B.E. and M.E. degrees in electrical and electronic engineering from Niigata University, Japan, in 2021 and 2023. He is currently working with NTT Access Network Service Systems Laboratories.

His research interests include millimeter-wave radio channel sounding and modeling. He is a member of the IEICE.

Naoya Suzuki received the B.E. degree in electrical and electronic engineering from Niigata University, Japan, in 2022, where he is currently pursuing the M.E. degree. His research interests include millimeter-wave radio channel sounding and modeling. He is a Student Member of the IEICE.

Banibrata Bag has received his BE in Computer Science & Engineering from Dr. B.C. Roy Engineering College, Durgapur, India, in 2004 and M.Tech in Electronics and Communication Engineering from Techno Main Salt Lake, Kolkata, India, in 2009. He joined as an assistant professor in the department of Electronics and Communication Engineering, Haldia Institute of Technology, Haldia, India, in 2010. He obtained his PhD degree from Jadavpur University, Kolkata, India, in 2022. Currently, he is working as a Specially Appointed Assistant Professor at the Graduate School of Science and Technology, Niigata University, Japan. His current research interests include millimeter-wave and terahertz radio propagation channel modeling and optical wireless communications.

Riku Takahashi received his B.E. degree in Electrical and Electronic Engineering from Niigata University, Japan, in 2022, where he is currently pursuing his M.E. degree. His research interests include millimeter-wave and terahertz radio channel sounding and modeling. He is a Student Member of the IEICE.

Minseok Kim (S'02–M'05-SM'18) was born in Seoul, Korea. He received the B.S. degree in Electrical Engineering from Hanyang University, Seoul, Korea, the M.E. and D.E. degrees in Division of Electrical and Computer Engineering, Yokohama National University (YNU), Japan in 1999, 2002, and 2005, respectively. In 2007, he was an Assistant Professor with the Tokyo Institute of Technology, Tokyo, Japan and a Visiting Scholar with the Georgia Institute of Technology, Atlanta, GA, USA, in 2010. In 2014, he joined the Graduate School of Engineering, Niigata University, Niigata, Japan, as an Associate Professor.

His current research interests include radio propagation channel measurement and modeling, millimeter-wave radar, radio tomographic imaging techniques, and MIMO/antenna array signal processing. He is a Senior Member of the IEICE. He is also serving as an Associate Editor for *IEEE Access* and *IEEE Antennas Wirel. Propag. Lett.*.